

Blue straggler stars beyond the Milky Way. IV. Radial distributions and dynamical implications

CHENGYUAN LI,^{1,2,3} WEIJIA SUN,^{4,5} JONGSUK HONG,⁵ LICAI DENG,⁶ RICHARD DE GRIJS,^{1,2,7} AND ALISON SILLS⁸

¹*Department of Physics and Astronomy, Macquarie University, Balaclava Road, Sydney, NSW 2109, Australia*

²*Research Centre for Astronomy, Astrophysics and Astrophotonics, Macquarie University, Balaclava Road, Sydney, NSW 2109, Australia*

³*Department of Astronomy, China West Normal University, Nanchong 637002, China*

⁴*Department of Astronomy, Peking University, Yi He Yuan Lu 5, Hai Dian District, Beijing 100871, China*

⁵*Kavli Institute for Astronomy and Astrophysics, Peking University, Yi He Yuan Lu 5, Hai Dian District, Beijing 100871, China*

⁶*Key Laboratory for Optical Astronomy, National Astronomical Observatories, Chinese Academy of Sciences, 20A Datun Road, Beijing 100012, China*

⁷*International Space Science Institute–Beijing, 1 Nanertiao, Zhongguancun, Hai Dian District, Beijing 100190, China*

⁸*Department of Physics and Astronomy, McMaster University, 1280 Main Street West, Hamilton, ON, L8S 4M1 Canada*

Submitted to ApJ

ABSTRACT

Blue straggler stars have been proposed as powerful indicators to measure the dynamical state of Galactic globular clusters. Here we examine for the first time if this framework of blue straggler stars as dynamical clocks, which was specifically developed for Galactic globular clusters, may also hold for younger globular clusters in the Large Magellanic Cloud. Using *Hubble Space Telescope* observations, we study seven Large Magellanic Cloud star clusters with ages between ~ 700 Myr and 7 Gyr. We confirm that our sample clusters are consistent with the empirical correlation previously derived for Galactic globular clusters, within a modest tolerance. We suggest that to further examine if blue straggler stars can measure the dynamical state of their host clusters over an extended range of dynamical ages, more studies of dynamically older Magellanic Cloud clusters are required. We discuss the physical implications of our results in terms of their central, dimensionless King potential, as well as the initial retention fraction of black holes.

Keywords: blue stragglers — galaxies: star clusters — Magellanic Clouds — stars: kinematics and dynamics

1. INTRODUCTION

In dense stellar systems like globular clusters (GCs), blue straggler stars (BSSs) represent examples of the bluest and brightest populations. They lie on an extension of the main-sequence (MS) (e.g., Sandage 1953; Ferraro et al. 1993; Li et al. 2013b) in the color–magnitude diagram (CMD). BSSs are thought to be more massive than the bulk of the ‘normal’ stars (e.g., Fiorentino et al. 2014) in star clusters. They are exotic objects which may have been produced through active stellar dynamics — either through mergers of binary components (Hills & Day 1976; Andronov et al. 2006) or through direct collisions in dense clusters (McCrea 1964). Therefore, BSSs

can in principle reveal information about the dynamical processes in star clusters.

BSSs were found to be ideal probes of the dynamical history of Galactic GCs (e.g., Alessandrini et al. 2016; Lanzoni et al. 2016; Ferraro et al. 2018). The detection of bifurcated BSS populations in some post-core-collapse clusters strongly indicates that stellar collisions driven by cluster core collapse could produce BSSs within a short period of time (e.g., Ferraro et al. 2009; Dalessandro et al. 2013; Simunovic et al. 2014). Ferraro et al. (2012); Lanzoni et al. (2016) derived an empirical correlation between the radial distributions of BSSs and the dynamical ages of their host clusters in the Milky Way, which was recently underpinned by Ferraro et al. (2018). These authors concluded that the radial distributions of BSSs can serve as a ‘dynamical clock’ for measuring the dynamical states reached by GCs.

Since BSSs are closely related to binary evolutions, their spatial segregation may show consistency with that of a cluster’s binary population. An exploration of this type of correlation has been carried out over the last decade: the radial distribution of binary systems is indeed similar to that of the BSSs in star clusters (Milone et al. 2012; Geller et al. 2013). In some young massive clusters, the radial behavior of the binary systems is more complicated, because the ongoing dynamical binary disruption may mask their mass segregation (Li et al. 2013a; Geller et al. 2015; Yang et al. 2018). It is thus interesting to explore the radial behavior of BSSs in clusters younger than most Galactic GCs (~ 10 Gyr).

Although the framework describing how BSSs can probe the dynamical processes of their host stellar systems has been well-studied for Galactic GCs, whether our understanding of BSSs would also hold for their younger, extragalactic counterparts remains unclear. A limited number of studies aiming to explore BSSs in star clusters in the Magellanic Clouds have recently been carried out. Li et al. (2013b) detected two separated groups of BSSs in the CMD of the Large Magellanic Cloud (LMC) GC Hodge 11, which is similar (but less significant) to the bifurcations found in some Galactic GCs (Ferraro et al. 2009; Dalessandro et al. 2013; Simunovic et al. 2014). Recently, the young (1–2 Gyr-old) LMC cluster NGC 2173 was found to exhibit two well-separated BSS sequences in its CMD (Li et al. 2018a), a feature which is commonly explained as the result of a cluster’s core collapse. However, the number density profile of NGC 2173 does not exhibit a central cusp, a typical feature created by a collapsed core. For another 1–2 Gyr-old cluster, NGC 2213, Li & Hong (2018) found that the radial distribution of its BSSs is consistent with that of the normal stars, showing no evidence of dynamical mass segregation (although dynamical calculations carried out for that cluster showed that the radial distribution of its BSSs should have been shaped by dynamical mass segregation). Li & Hong (2018) suggested that this may be because the presence of some extremely compact objects such as black holes in the cluster’s central region could have delayed the dynamical evolution of the BSSs. Sun et al. (2018) studied BSSs in 25 Magellanic Cloud star clusters. They revealed a sublinear correlation between the number of BSSs in the cluster cores and the clusters’ core masses, i.e., $N_{\text{BSS},c} \propto M_c^{0.66 \pm 0.07}$, where $N_{\text{BSS},c}$ and M_c are the number of BSSs in the core region and the cluster’s core mass, respectively. This feature had been previously confirmed in Galactic GCs (Knigge et al. 2009), which implied that binary evolution is the major formation channel of BSSs.

In this paper, we study seven LMC massive clusters with ages from ≤ 1 Gyr to ~ 7 Gyr. Using diagnostic diagrams similar to those used by Lanzoni et al. (2016), we examine if the BSS mass segregation degrees could be applied to measure the dynamical states of their host clusters. The effects of (small-)number dispersions of the BSSs as well as of field contamination are carefully explored by employing a Monte-Carlo based statistical examination. We will show that our result is generally consistent with the empirical relationship derived by Lanzoni et al. (2016) and Ferraro et al. (2018) for Galactic GCs. We discuss the physical implications of our results by comparing our observations with the numerical simulation results of Alessandrini et al. (2016).

We introduce the details of the observations and the data reduction in Section 2. The main results of our analyses are presented in Section 3. In Section 4, we provide a discussion of the physical implications of our results. Section 5 contains a summary and our conclusions.

2. DATA REDUCTION

2.1. Star cluster selection

We first examined all LMC clusters contained in the *Hubble Space Telescope* (HST) archive data set¹ using the cluster catalog of Baumgardt et al. (2013). We selected data sets observed with the HST Ultraviolet and Visible channel of the Wide Field Camera 3 (UVIS/WFC3) or the Wide Field Channel of the Advanced Camera for Surveys (ACS/WFC). We then performed point-spread-function (PSF) photometry on the calibrated scientific image frames (with extension ‘fit’) using the WFC3 or ACS modules of the DOLPHOT 2.0 package (Dolphin 2016). After having obtained the raw stellar catalog, we employed the same method as Li et al. (2018b) to filter out ‘bad’ detections and compile the ‘clean’ catalogs. Here, bad detections are objects which were identified as bad pixels, cosmic rays, extended sources, or centrally saturated objects. Objects with unrealistic sharpness or which were strongly affected by their nearby crowded environment were removed as well (for details, see Li et al. 2018b). In this paper, we only focus on BSSs and normal evolved stars, such as red-giant branch (RGB) stars, asymptotic giant branch (AGB) stars and red clump (RC) stars. All these stars have high signal-to-noise ratios (SNR > 250); only central saturation will reduce their completeness levels. We confirm that fewer than 5% of the stars of interest would be removed by our data reduction procedures.

¹ <https://archive.stsci.edu/hst/search.php>

In this paper, we aim to examine if the framework developed by Ferraro et al. (2012) and Lanzoni et al. (2016) for BSSs in old Galactic GCs could also apply to younger GCs (younger than ~ 10 Gyr). Therefore, we do not perform photometry on clusters older than 10 Gyr. For clusters younger than 10 Gyr, we only selected clusters containing more than 10 BSS candidates for reasons of statistical robustness. These selection criteria forced us to exclude some young clusters, because those clusters do not show a clear turnoff region and their BSSs evolve too fast to be captured in an observational snapshot.

It is possible that some BSS candidates are just field stars, which may occasionally be located along the line-of-sight direction. To obtain reliable results about the radial distributions of BSSs, field-star decontamination is required. However, because of the large distances to the LMC clusters (e.g., de Grijs et al. 2014), using proper motions to reduce pollution by field stars is not possible². Therefore, we have visually inspected the spatial distributions of the selected BSSs for each cluster. If these stars did not show any clear central concentration, we did not analyze the cluster. Finally, only seven clusters were selected for further study. Table 1 lists the basic observational information for our seven sample clusters, as well as that of their associated parallel observations centered on nearby regions (if any), which are used as reference fields.

2.2. Selection of the stellar samples

In Fig. 1 we present the processed CMDs of our clusters, along with their best-fitting isochrones calculated based on the PARSEC stellar evolution code (Bressan et al. 2012). For each cluster, we use an old isochrone to fit the bulk stellar population based on visual inspection. Most clusters exhibit an extended main-sequence turnoff (eMSTO) region, a feature that is commonly found in clusters younger than ~ 1 – 2 Gyr (e.g., Milone et al. 2009; Marino et al. 2018). The eMSTO makes determining an exact age for the bulk stellar population difficult. However, some intermediate-age clusters with eMSTO regions exhibit tight subgiant branches (SGBs; Li et al. 2014; Bastian & Niederhofer 2015). Therefore, we adopt the isochrone that approximately describes the SGB ridge-line as the best-fitting isochrone. If a cluster does not show a well-populated SGB, we adopt an

isochrone that describes the blue boundary of the turnoff region as the best-fitting isochrone. To search for a cluster’s BSSs, we adopted another young isochrone characterized by a turnoff stellar mass twice that of the old isochrone. Both isochrones were calculated for the same metallicity, extinction, and distance modulus; their only difference are their respective ages. Parameters for the adopted isochrones are presented in Table 2, where we have included the mass of the old isochrones’ turnoff stars as well. NGC 2213 was recently studied by Li & Hong (2018); we directly apply these authors’ best-fitting isochrones to fit its CMD.

2.2.1. Blue straggler stars

The next step involved selecting BSSs and their reference stellar populations, which is similar to Lanzoni et al. (2016)’s approach to study their Galactic GCs. For most clusters, the reference stellar populations are composed of RGB, RC, and AGB stars. Since the RGB and AGB are poorly populated in NGC 1831 and NGC 1868, we only selected the populations of RC stars as these clusters’ reference populations. Our BSS selection approach proceeded as follows.

1. We shifted each cluster’s old isochrone to run across the region where the stellar number density is significantly lower than that in the MSTO region. Specifically, the position of this boundary was determined as follows. We first determined the best-fitting old isochrone describing the red boundary of the BSS region. We then checked how many stars would be selected as BSS candidates. We then shifted this isochrone adopting color steps of ~ 0.01 mag to the blue. The number of selected BSS candidates would initially decrease rapidly, because many MSTO stars were removed. Once the rate of the decrease dropped below 5% per 0.01 mag, we defined the shifted isochrone as the boundary separating BSSs from MSTO stars. We emphasize that this method was adopted to minimize the number uncertainties. In reality, one would not expect a sharp boundary between BSSs and MSTO stars, and there are probably collision products and binary mass transfer products mixed in with MS stars.
2. We defined stars located along the extension of the MS that were bluer than the red boundary of the MSTO region but redder than the young isochrone combined with a negative photometric color spread (which was determined to take the photometric uncertainties and possible differential reddening into account, see Li et al. 2018b) as our BSS sample.

² Most BSSs in our LMC clusters have magnitudes between 17 and 20 mag in the *Gaia* *G* band. The typical proper motion uncertainty for these stars is 0.2–1.2 mas yr⁻¹ (see <https://www.cosmos.esa.int/web/gaia/dr2>). At the distance of the LMC, ~ 50 kpc, this corresponds to ~ 50 – 300 km s⁻¹, which is much larger than the central velocity dispersion of an LMC star cluster (< 5 km s⁻¹ McLaughlin & van der Marel 2005).

Table 1. Description of the observations used. Clusters are ranked in terms of increasing best-fitting isochronal ages (see Table 2)

Cluster	Camera	Exposure time	Filter	Program ID	PI name
NGC 1831 (Cluster & Field)	UVIS/WFC3	2×975 s + 2×1115 s 100 s + 660 s + 720 s	F336W F814W	GO-14688	P. Goudfrooij
NGC 1868 (Cluster & Field)	UVIS/WFC3	2×830 s + 831 s 90 s + 666 s	F336W F814W	GO-14710	A. P. Milone
NGC 2173 (Cluster)	UVIS/WFC3	120 s + 2×700 s 30 s + 550 s + 2×700 s	F475W F814W	GO-12275	L. Girardi
NGC 2173 (Field)	ACS/WFC	90 s + 2×500 s + 2×700 s 10 s + 600 s + 690 s + 2×700 s	F475W F814W	GO-12257	L. Girardi
NGC 2203 (Cluster)	UVIS/WFC3	120 s + 2×700 s 30 s + 550 s + 2×700 s	F475W F814W	GO-12275	L. Girardi
NGC 2203 (Field)	ACS/WFC	90 s + 2×500 s + 2×700 s 10 s + 550 s + 690 s + 2×713 s	F475W F814W	GO-12257	L. Girardi
NGC 2213 (Cluster)	UVIS/WFC3	120 s + 600 s + 720 s 30 s + 2×700 s	F475W F814W	GO-12275	L. Girardi
NGC 2213 (Field)	ACS/WFC	2×500 s 2×500 s	F475W F814W	GO-12257	L. Girardi
NGC 1651 (Cluster)	UVIS/WFC3	120 s + 600 s + 720 s 30 s + 550 s + 2×700 s	F475W F814W	GO-12275	L. Girardi
NGC 1651 (Field)	ACS/WFC	90 s + 2×500 s + 2×700 s 30 s + 2×700 s	F475W F814W	GO-12257	L. Girardi
ESO 121-SC03 (Cluster & Field)	ACS/WFC	90 s + 3×360 s 8 s + 2×350 s	F435W F814W	GO-10595	P. Goudfrooij

Table 2. Basic model fit parameters.

Cluster	$\log t_1$ [yr] (1)	$\log t_2$ [yr] (2)	Z^* (3)	A_V (mag) (4)	$(m - M)_0$ (mag) (5)	M_{TO} (M_\odot) (6)
NGC 1831	8.85	8.05	0.006	0.12	18.50	2.21
NGC 1868	9.08	8.20	0.006	0.06	18.50	1.82
NGC 2173	9.25	8.45	0.008	0.16	18.45	1.62
NGC 2203	9.25	8.49	0.006	0.22	18.50	1.59
NGC 2213	9.26	8.48	0.006	0.06	18.50	1.59
NGC 1651	9.30	8.52	0.005	0.30	18.55	1.50
ESO 121-SC03	9.84	9.00	0.001	0.27	18.40	0.94

(1) Age of the bulk population stars (in logarithmic units). (2) Age of the young isochrone (3) Metallicity. (4) Reddening. (5) Distance modulus. (6) Turnoff stellar mass for the bulk population

*: $Z_\odot = 0.0152$.

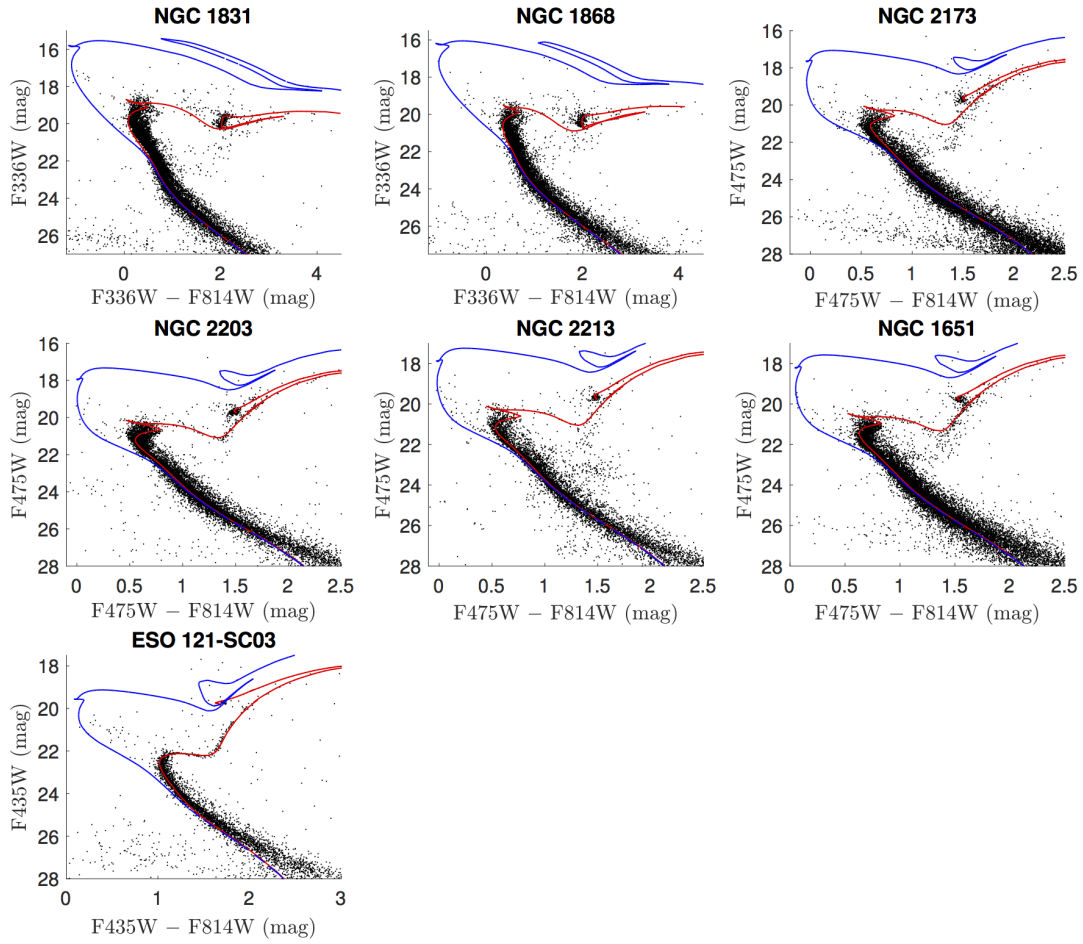


Figure 1. Processed CMDs for all clusters. Red solid lines are isochrones describing the bulk stellar populations of the star clusters. Blue dashed lines are the corresponding young isochrones with turnoff stellar masses twice those of the old isochrones.

3. We also adopted a lower magnitude limit for our BSSs. To avoid contamination by MS stars, we adopted the locus where the young and old isochrones begin to diverge significantly (their color separations are greater than at least 0.1 mag) as our lower boundary.
4. We do not set any upper boundary for our BSSs, because we found that the adopted young isochrone covers all observed stars brighter than the MSTO region.

2.2.2. Reference population stars

For NGC 1831 and NGC 1868, we only selected RC stars as reference stellar populations, because there are no well-populated RGB or AGB features in their CMDs (see Fig. 1). For these two clusters, we simply defined a box which approximately covered the bulk of their RC stars as the typical RC region. For the other clusters, a combination of RGB, RC, and AGB stars was selected as reference population. This is similar to the approach adopted by Lanzoni et al. (2016), who defined stars on the RGB, SGB, and/or horizontal branch as reference populations. To select reference populations in our other clusters, we used the CMD section following the bottom of the RGB of the old isochrone as the ridge-line. We then applied a large color–magnitude spread to define the relevant boundary; the typical magnitude deviation from the ridge-line was about 0.1–0.3 mag, which we adopted so as to consider the possible scatter caused by photometric errors and differential reddening. We illustrate our selection method in Fig. 2. We also assumed that there are number uncertainties associated with the normal distributions defining these stellar populations.

2.3. Structural parameters

We calculated the center coordinates of our clusters using the method described by Li et al. (2018a). We calculated the stellar number density contours for the stars detected in the field of view (FoV) of our observations. The position where the stellar number density reaches its maximum value was defined as the cluster center. The stellar spatial distributions of our clusters, as well as their number density contours and the derived cluster centers, are presented in the left-hand panels of Figs 3–8. For NGC 2213, we used the cluster center determined by Li & Hong (2018). We calculated the clusters’ brightness profiles in two passbands. Because massive stars are expected to contribute most of the flux, in each passband we only selected stars brighter than a given magnitude to calculate their brightness profiles. This magnitude limit varied from cluster to cluster; it was usually two or three magnitudes brighter than the detection limit.

We only selected these bright stars because, they are all characterized by high completeness levels. We calculated their brightness profiles using the method adopted by Li & Hong (2018). If a cluster had a separate field observation, we also extended their brightness profile to the field region, adopting a constant brightness level. Using least-squares minimization, we used a King model to fit the calculated brightness profile (King 1962):

$$\mu(r) = k \left[\frac{1}{\sqrt{1 + (r/r_c)^2}} - \frac{1}{\sqrt{1 + (r_t/r_c)^2}} \right] + b. \quad (1)$$

Here, r_c and r_t are the core and tidal radii, respectively, b is a constant representing the background brightness, and k is a normalization coefficient. The calculated brightness profiles as well as the best-fitting King models are shown in the right-hand panels of Figs 3–8 (for NGC 2213, see Li & Hong 2018, their Fig. 3).

Based on the best-fitting King models, we also determined the best-fitting half-light radii in both passbands. These derived structural parameters are presented in Table 3. For most of our clusters, we found that the derived structural parameters are consistent within the uncertainties. We thus selected their average values as the best-fitting structural parameters.

In this paper, we only analyze stars within the half-light radius, which we adopt as the cluster region. For NGC 1831, NGC 1868, and ESO 121-SC03, there are no separate observations for use as reference field. We adopted the regions at radii greater than 20 pc as our reference fields. As shown in Table 3, these radii are too small compared with the corresponding tidal radii. This means that we must have overestimated the field contamination for NGC 1831, NGC 1868, and ESO 121-SC03. In principle, overestimation of the field contamination would not affect the derived radial distributions of their BSSs, because we have assumed a flat distribution of field stars in our analysis. However, it will increase the associated uncertainties when we calculate their central concentrations (see Section 3). For NGC 2173, NGC 2203, NGC 2213, and NGC 1651, parallel observations located beyond the tidal radii were used as reference fields. The selected field stars are shown in Fig. 9. However, this figure cannot reflect the actual field contamination level, because the field areas are much larger than the cluster regions. In Table 4, we list the area ratios of the reference fields and the cluster regions. To show that the derived radial BSS distributions are not field artefacts, we also confirmed that all BSSs in our clusters show apparent central concentrations (see Fig. 10), whereas the adopted field stars do not.

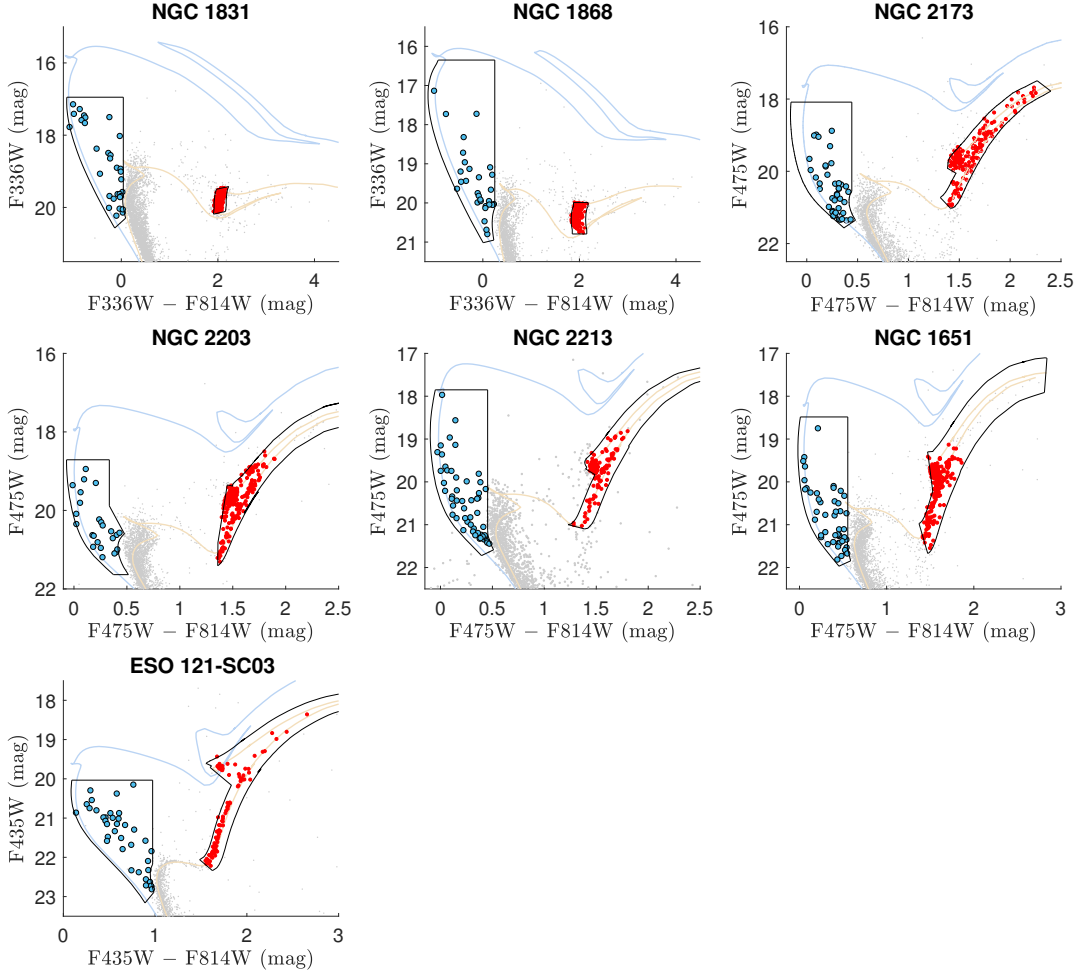


Figure 2. Illustration of how we select BSSs (blue circles) and reference population stars (RGB, RC, and AGB stars; indicated by red dots).

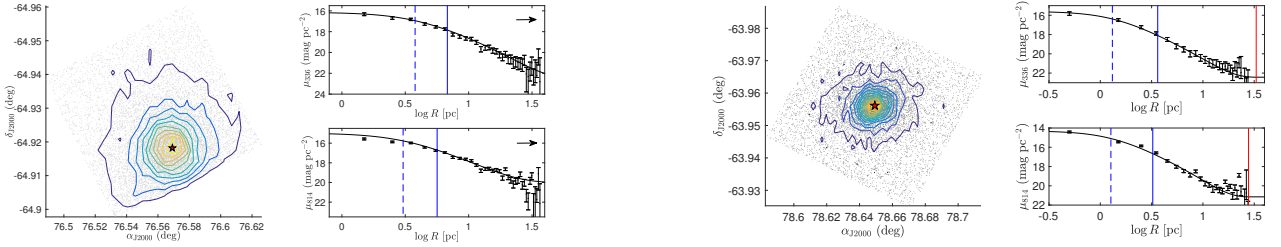


Figure 3. (left) Stellar spatial distribution and number density contours for NGC 1831. The red pentagram is the calculated cluster center. (right) Brightness profile of NGC 1831 in two passbands (top: F336W; bottom: F814W). Blue dashed and solid lines indicate the best-fitting core and half-light radii. Black arrows mean that the best-fitting tidal radii associated with these profiles are beyond the figure boundaries.

Figure 4. As Fig. 3, but for NGC 1868. In the right-hand panels, red solid lines indicate the best-fitting tidal radii in both passbands.

2.4. Stellar completeness

The next step is to correct for the differences in completeness between the stellar samples in the cluster regions and the reference fields. For NGC 1831, NGC

Table 3. Best-fitting structural parameters based on King profile fits. (1) Cluster name, (2) right ascension, (3) declination, (4) best-fitting core radius in band A, (5) best-fitting half-light radius in band A, (6) best-fitting tidal radius in band A, (7) best-fitting core radius in band B, (8) best-fitting half-light radius in band B, (9) best-fitting tidal radius in band B. Here, ‘band A’ is either F336W, F435W, or F475W, while ‘band B’ is F814W. Problematic values or uncertainties are indicated in bold font; they were not used. The structural parameters of NGC 2213 were derived by Li & Hong (2018) (only calculated in the F475W passband).

Cluster (1)	α_{J2000} (2)	δ_{J2000} (3)	r_{1c} (pc) (4)	r_{1hl} (pc) (5)	r_{1t} (pc) (6)	r_{2c} (pc) (7)	r_{2hl} (pc) (8)	r_{2t} (pc) (9)
NGC 1831	05 ^h 06 ^m 16.56 ^s	-64°55′05.52″	3.78±0.22	6.79 ^{+2.36} _{-3.67}	60.86±45.20	3.04±0.21	5.64 ^{+1.37} _{-0.34}	52.12 ± 24.79
NGC 1868	05 ^h 14 ^m 35.88 ^s	-63°57′21.96″	1.31±0.12	3.63 ^{+0.31} _{-0.37}	33.06±7.73	1.27±0.20	3.25 ^{+0.45} _{-0.49}	27.83±5.28
NGC 2173	05 ^h 57 ^m 58.68 ^s	-72°58′41.52″	3.01±0.40	8.53 ^{+1.67} _{-2.53}	84.27±48.57	2.84±0.44	7.61 ^{+1.81} _{-2.13}	74.56±43.74
NGC 2203	06 ^h 04 ^m 42.60 ^s	-75°26′17.16″	4.64±0.15	9.40 ^{+0.30} _{-0.31}	63.99±4.55	4.78±0.37	8.62 ^{+0.59} _{-0.60}	52.28±7.88
NGC 2213	06 ^h 10 ^m 42.24 ^s	-71°31′44.76″	1.45±0.02	3.59 ^{+0.41} _{-0.59}	31.41±3.02	–	–	–
NGC 1651	04 ^h 37 ^m 32.16 ^s	-70°35′09.60″	3.66±0.30	6.52 ^{+0.46} _{-0.45}	39.78±5.40	3.63±0.42	6.48 ^{+0.70} _{-0.72}	40.26±8.11
ESO 121-SC03	06 ^h 02 ^m 02.40 ^s	-60°31′23.52″	5.66±1.14	7.18 ^{+1.00} _{-1.01}	32.64±7.73	6.28±1.50	7.25 ^{+1.08} _{-1.04}	30.05±6.42

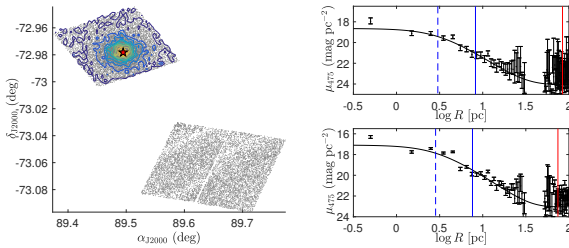


Figure 5. As Fig. 4, but for NGC 2173. The bottom square in the left-hand panel represents a nearby field observation.

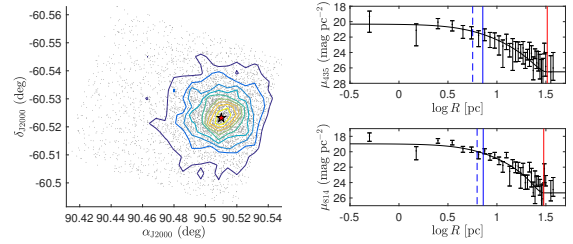


Figure 8. As Fig. 3, but for ESO 121-SC03.

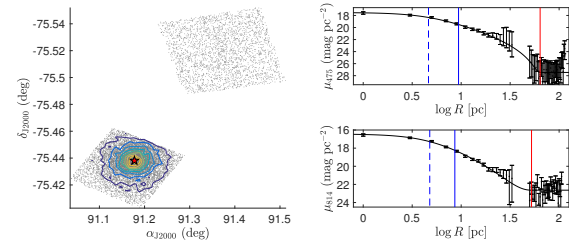


Figure 6. As Fig. 5, but for NGC 2203.

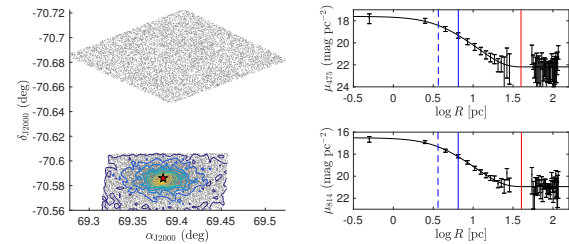


Figure 7. As Fig. 5, but for NGC 1651.

1868, and ESO 121-SC03, there are no significant completeness differences, because their reference fields and

cluster regions were observed as part of the same image. However, the reference fields associated with NGC 2173, NGC 2203, NGC 2213, and NGC 1651 may be characterized by significantly different completeness levels. Therefore, we have to calculate the completeness levels for all stellar samples in both the cluster regions and the reference fields. To do this, we generated 100,000 artificial stars with the same color–magnitude distributions to the selected stellar samples. We then repeated our DOLPHOT approach in *artificial star* mode 1,000 times. Each time we only photometered 100 artificial stars. We did not do the photometry for these 100,000 artificial stars at one time because adding too many stars to the raw images would increase the crowding in the FoV, unnecessarily reducing the stellar completeness. For clusters with a separate reference field, we also applied the *artificial star*-mode photometry to the field observations. For the resulting artificial stars, DOLPHOT provides the same photometric parameters (magnitudes, crowding, sharpness, etc.). We employed the same data reduction process to the artificial stars as to the real observations, obtaining a ‘clean’ catalog of artificial stars (see Section 2.1). The number ratio of the artificial stars in the re-

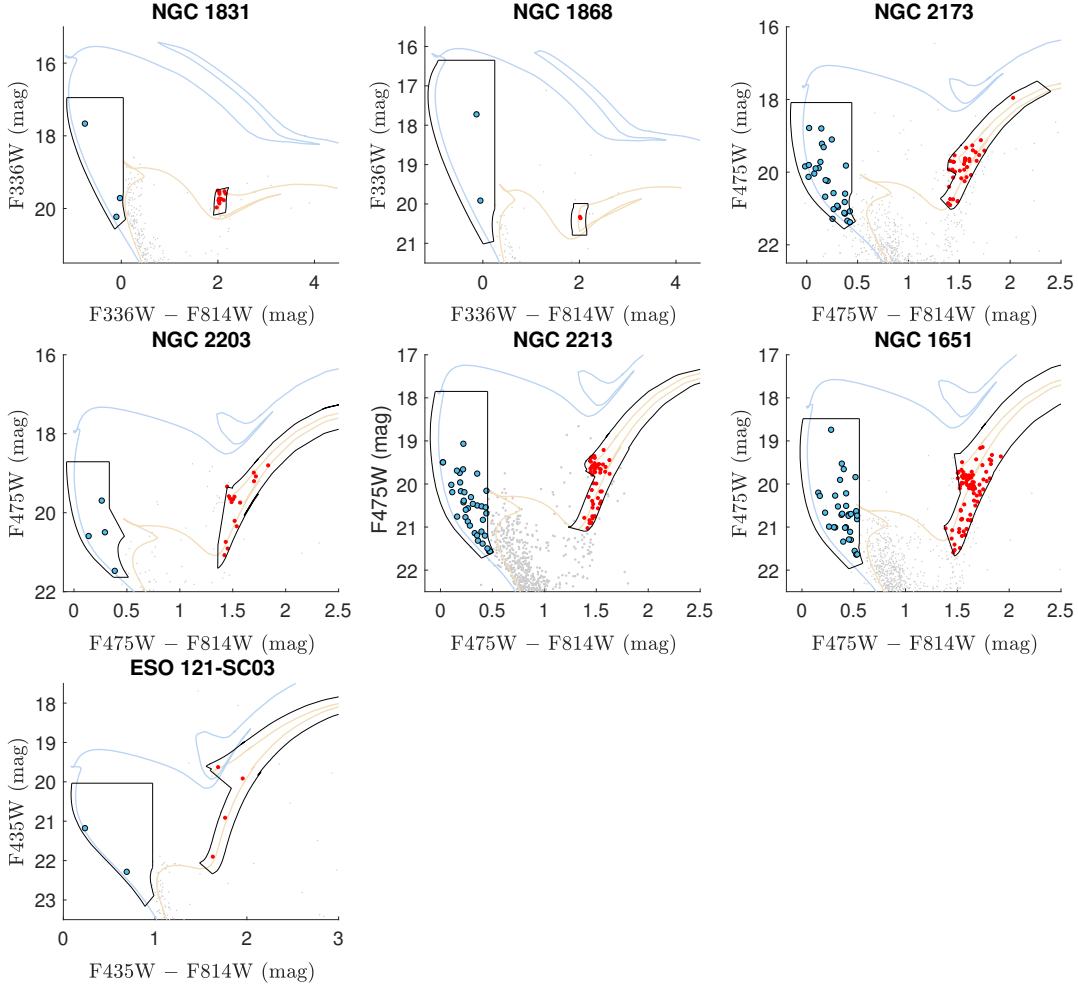


Figure 9. As Fig. 2, but for the observations of the corresponding reference fields. Note that the reference fields are larger than the cluster regions (see Table 4).

sulting ‘clean’ catalog and in the raw catalog defines the stellar completeness: see Table 4.

The completeness of most stellar samples in our clusters is almost unity. This is expected, since these stars have high SNRs (>250). By examining the sharpness distribution of these stars, we confirmed that they are unlikely extended sources (e.g., faint background galaxies) or sharp sources (such as cosmic rays). However, for NGC 2203 we found that the stellar completeness in the region of the reference population is only 49%. This is because some bright objects, such as the thermally pulsing AGB stars, are saturated. This also applies to the reference population stars in the reference fields of NGC 2213 and NGC 1651, which yield average completeness levels of 43% and 37%, respectively. By exploring the characteristic of the artificial stars, we

confirmed that this is because some stars in the F814W passband are saturated. If we constrain the reference population stars to $F814W \geq 16.5$ mag for NGC 2203, and $F814W \geq 17.0$ mag and $F814W \geq 17.4$ mag for the reference fields of NGC 2213 and NGC 1651, respectively, their overall completeness will be greater than 95%. As a consequence, for NGC 2203, NGC 2213, and NGC 1651, we only selected normal evolved stars fainter than these magnitude limits. This is why in Figs 2 and 9 the reference population stars seem to be cut off in magnitude. In Fig. 11 we show an example of the input (left-hand panel) and output CMDs for artificial stars generated for NGC 2203.

3. MAIN RESULTS

In this section we study the radial distributions of the BSSs in our sample clusters. [Alessandrini et al. \(2016\)](#)

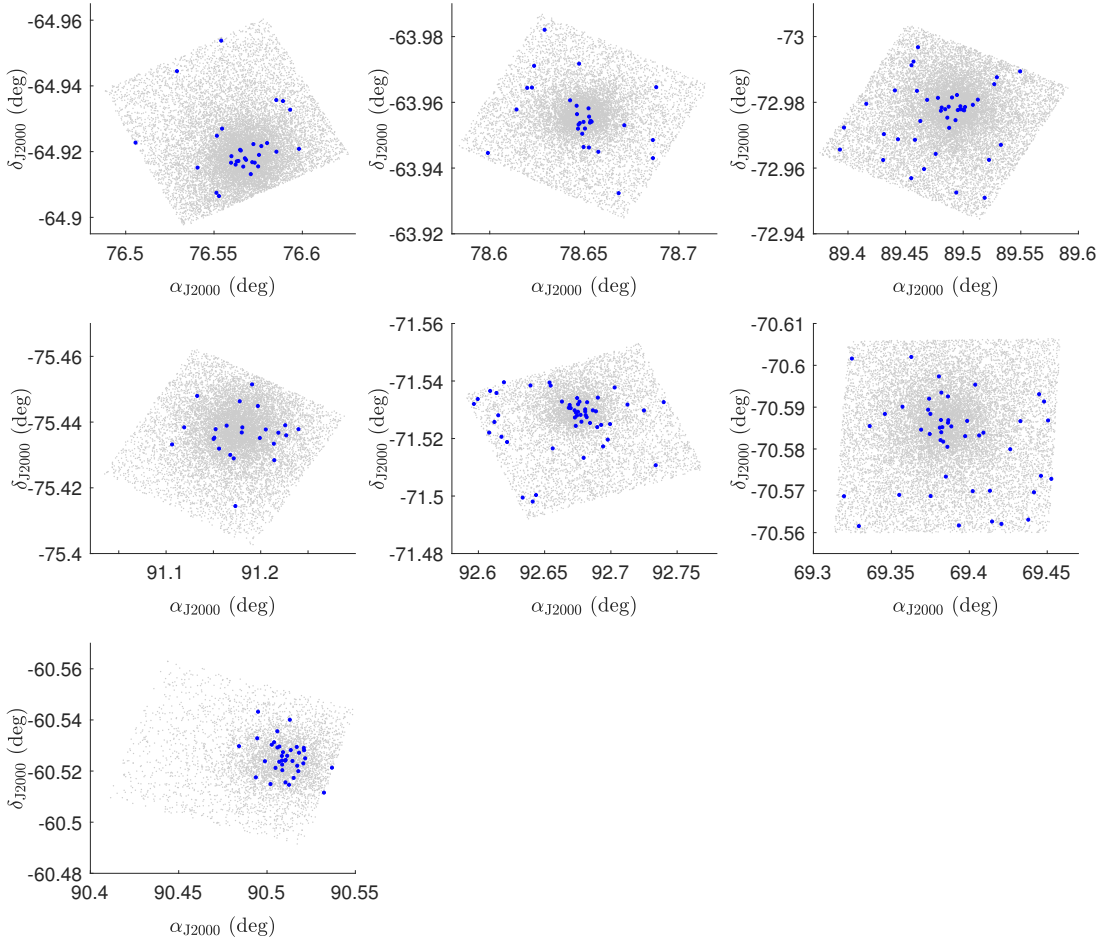


Figure 10. BSS spatial distributions (blue dots) in our sample clusters.

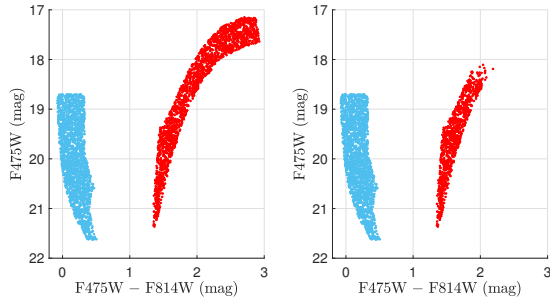


Figure 11. Input (left) and output (right) CMDs for artificial stars corresponding to NGC 2203. Blue and red dots represent the artificial BSSs and normal evolved stars (reference population stars). As shown in the right-hand panel, most normal evolved stars located in the upper RGB are saturated.

and Lanzoni et al. (2016) defined a parameter A_{rh}^+ , which represents the area enclosed between the cumulative ra-

dial distributions of the BSSs and the reference samples. Following their framework, we calculated A_{rh}^+ for the BSSs in our clusters. Specifically, A_{rh}^+ is defined as

$$A_{\text{rh}}^+ = \int_{-\infty}^0 \phi_{\text{b}}(x) - \phi_{\text{r}}(x) dx, \quad (2)$$

where $x = \log(r/r_{\text{hl}})$ is the logarithm of the radius from the cluster center normalized to the half-light radius r_{hl} ; $x = -\infty$ and $x = 0 = \log 1$ correspond to $r = 0$ and $r = r_{\text{hl}}$, $\phi_{\text{b}}(x)$ and $\phi_{\text{r}}(x)$ are the cumulative radial distributions of BSSs and reference population stars. A large value of A_{rh}^+ means that the BSSs are more centrally concentrated than the reference population stars. If A_{rh}^+ is equal to zero or even negative, this would indicate that the BSSs are fully mixed with the reference population stars, or even less segregated.

The uncertainty adopted for our calculation includes two components. The first comes from the normal distri-

Table 4. Completeness for different stellar samples and field-to-cluster area ratios. (1) Cluster name, (2) completeness of BSSs in the cluster area, (3) completeness of reference population stars (RGB, RC, and AGB stars) in the cluster area, (4) completeness of BSSs in the reference field, (5) completeness of reference population stars in the reference field, (6) area ratio of the reference field to the adopted cluster region.

Cluster (1)	f_b (2)	f_r (3)	f_{bf} (4)	f_{rf} (5)	A_f/A_c (6)
NGC 1831	99%	99%	–	–	4.7
NGC 1868	99%	99%	–	–	7.8
NGC 2173	99%	98%	~100%	97%	11.8
NGC 2203	~100%	49%	~100%	96%	9.3
NGC 2213	99%	95%	99%	43%	56.3
NGC 1651	~100%	98%	99%	37%	18.3
ESO 121-SC03	99%	97%	–	–	7.7

bution of the uncertainties in the stellar total number. The second part is caused by the unknown field contamination. For clusters beyond the Milky Way, only statistical methods are applicable to estimate the field contamination. This method compares the CMD of the cluster region with that of its reference field and statistically subtracts stars from the cluster CMD by assuming that field stars will have the same color–magnitude distribution in the cluster region. This method has been widely used for LMC clusters (e.g., Milone et al. 2018; Yang et al. 2018). However, it cannot be directly applied in this paper, because (1) both the numbers of genuine cluster members and contaminating field stars are very small in the BSS regions. The small number dispersion will lead to large uncertainties in the number ratios in different radial bins. (2) We aim to study the radial distribution of BSSs. Randomly subtracting a small number of field stars without careful consideration of their spatial positions may significantly change the result, thus reducing the reliability of our conclusion.

Because of these limitations, we devised a Monte-Carlo based method to estimate the ‘average’ number fraction radial profiles. Before applying this method, we first confirmed that the total number of BSSs in the cluster regions cannot be fully explained by field contamination. In Table 5 we list the observed number of BSSs and reference population stars in the cluster regions and the expected numbers of contaminating field stars (after correction for the area difference between cluster regions and the reference fields).

For both the populations of BSSs and reference stars, we randomly assigned N_f field stars to the cluster region for each cluster. Here, N_f is drawn randomly from

Table 5. Observed numbers of (2) BSSs and (3) reference population stars in the cluster regions, and the expected numbers of contaminating field stars in the regions of (4) BSSs and (5) reference population stars.

Cluster (1)	N_b (2)	N_r (3)	N_{bf} (4)	N_{rf} (5)
NGC 1831	19	107	1–2	~3
NGC 1868	11	84	~0	~0
NGC 2173	19	126	~2	~3
NGC 2203	13	242	0–1	1–2
NGC 2213	18	61	0–1	~1
NGC 1651	19	122	1–2	4–5
ESO 121-SC03	27	52	~0	0–1

a normal distribution centered on the expected number of field stars. The spatial distribution of these artificial field stars is homogeneous. We next subtracted these field stars from the observed sample of both BSSs and reference stars and calculated the ‘field-subtracted’ cumulative profiles. We emphasize again that the resulting radial distribution could strongly depend on the positions of the subtracted field stars when the number of field stars is small. Therefore, we repeated this procedure 1,000 times and adopted the average cumulative profiles of each sample as the final result. We then examined how this would change the resulting A_{rh}^+ . Our final A_{rh}^+ values are the averages of these 1,000 realizations. The associated uncertainty covers 95% of all runs. Our results are illustrated in Fig. 12 and listed in Table 6.

From Fig. 12 we find that the radial distributions of BSSs in these LMC clusters vary. In NGC 1831, NGC 2173, NGC 1651, and ESO 121-SC03, the BSSs are marginally more centrally concentrated than the normal evolved stars. In NGC 1868, NGC 2203, and NGC 2213, the radial distributions of the BSSs are very dispersed, showing no evidence of apparent mass segregation. We estimated the dynamical ages of the turnoff stars within the half-mass radii of our clusters. We confirmed that they are all dynamically older than at least one half-mass relaxation timescale (see the below). This is in contrast to the GCs in the Milky Way, where Ferraro et al. (2018) found that among 27 Galactic GCs observed as part of the *HST* UV Legacy Survey, 17 have BSS A_{rh}^+ greater than 0.18. We also applied the nonparametric k -sample ($k = 2$) Anderson–Darling test to check whether the cumulative distributions of BSSs and reference population stars are drawn from the same underlying distribution (our null hypothesis). We found that we

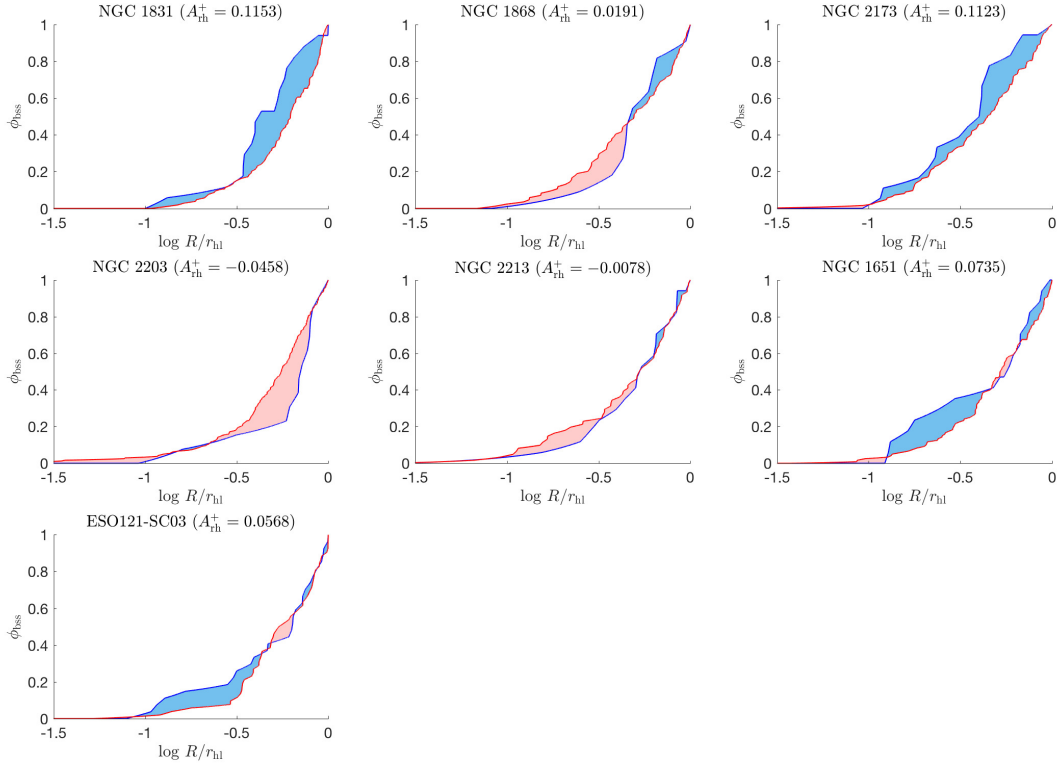


Figure 12. Cumulative curves normalized to r_{hl} for BSSs (blue lines) and reference population stars (red lines). The area enclosed between these two curves is defined as A_{rh}^+ , as indicated by the blue shaded region (positive contribution to A_{rh}^+) and pink shaded region (negative contribution to A_{rh}^+).

cannot reject the null hypothesis at a significance level of $p = 0.05$.

Lanzoni et al. (2016) and Ferraro et al. (2018) showed that A_{rh}^+ can measure the dynamical states of GCs in the Milky Way. In this paper, we examined if their conclusion also hold for our sample of younger GCs in the LMC. To do so, we use the formula introduced by Meylan (1987a) to calculate the half-mass relaxation timescales,

$$t_{\text{rh}} = 8.92 \times 10^5 \frac{M_{\text{total}}^{1/2}}{\bar{m}} \frac{r^{3/2}}{\log(0.4M_{\text{total}}/\bar{m})} \text{yr}, \quad (3)$$

where M_{total} is the cluster's total mass, \bar{m} is the typical mass for the stars of interest (in units of M_{\odot}), and r is the half-mass radius of interest. We assume that the half-light radius derived here, r_{hl} , is equal to the half-mass radius. In principle, we have adopted a three-dimensional (3D) radius under the assumption that our clusters are simple spherical systems. In principle, the real 3D radius is $4/3$ times the observed 2D projected radius (Spitzer 1987). M_{total} and \bar{m} were evaluated as follows. We first selected a sample of stars within the half-light radius. For this stellar sample, we calculate

the number of stars within a range of F814W magnitude that is of order 2–3 mag above the detection limit. We converted this magnitude range into a stellar mass range by interpolation of the best-fitting isochrone. We assumed that stars in this mass range follow a Kroupa mass function (Kroupa 2001) and then evaluated the total number of stars by extrapolating this mass function down to $0.08M_{\odot}$. The total mass for these stars thus represents half of the cluster total, since we have assumed that the half-light radius is equal to the half-mass radius. The average stellar mass is the total mass of all stars divided by their total number.

Using the equation

$$t_{\text{r0}} = 1.55 \times 10^7 \frac{1/\bar{m}}{\log(0.5M_{\text{total}}/\bar{m})} v_0 r_c^2 \text{yr}, \quad (4)$$

we calculated the central relaxation time (Meylan 1987a). Here v_0 is the central velocity scale in units of km s^{-1} , which we assumed to be equal to the core velocity dispersion,

$$v_0 = \sigma_0 = \sqrt{\frac{2GM_c}{r_c}}. \quad (5)$$

The estimation of the core mass, M_c , is similar to that of the total mass.

In Table 6, we present the calculated cluster total masses, stellar average masses, half-light and central relaxation times, as well as the BSSs' A_{rh}^+ . The associated uncertainties in the clusters' total masses and their relaxation times are linked to the uncertainties in the structural parameters. The average stellar mass does not have an associated uncertainty, because it only depends on the adopted mass function (we assumed a Kroupa mass function).

Lanzoni et al. (2016) measured the dynamical states of Galactic GCs based on the logarithm of the ratio of a cluster's central relaxation time and the Hubble time (13.7 Gyr), $\log t_{\text{r0}}/t_{\text{H}}$. However, this definition can only apply to GCs because almost all Galactic GCs have ages close to the Hubble time. The typical ages of our clusters span the range from less than 1 Gyr (NGC 1831) to ~ 7 Gyr (ESO 121-SC03). Therefore, to appropriately define the dynamical states of these younger GCs, we replaced the Hubble time with their isochronal ages, $\log t_{\text{r}}/t_{\text{iso}}$, where the isochronal ages are the ages associated with the best-fitting isochrones for the bulk population stars.

In Fig. 13 we show the $A_{\text{rh}}^+ - \log t_{\text{r0}}/t_{\text{iso}}$ diagrams for BSSs in these seven clusters. To make a direct comparison, the same diagram for 25 Galactic GCs is plotted as well (note that for these clusters their x positions are $\log t_{\text{r0}}/t_{\text{H}}$). As shown in Fig. 13, there is no obvious correlation between A_{rh}^+ and $\log t_{\text{r0}}/t_{\text{iso}}$ for these seven clusters. We have calculated the Pearson coefficient between A_{rh}^+ and $\log t_{\text{r0}}/t_{\text{iso}}$, which is 0.23. To check the relevant significance, we generated seven points randomly distributed in the diagrams and calculated their Pearson coefficient. We repeated this procedure 10,000 times and counted how many times we obtained a Pearson coefficient with a smaller absolute value than obtained for the observations. We defined this count divided by 10,000 as the significance of the correlations. This yields only 40%. For comparison, the Pearson coefficient for the correlation $A_{\text{rh}}^+ - \log t_{\text{r0}}/t_{\text{H}}$ for the 25 Galactic GCs studied by Lanzoni et al. (2016) is -0.85 , with a significance of 99%. Clearly, the correlation $A_{\text{rh}}^+ - \log t_{\text{r0}}/t_{\text{iso}}$ for Galactic GCs is much tighter than for the LMC clusters. The lack of a tight correlation between A_{rh}^+ and $\log t_{\text{r0}}/t_{\text{H}}$ for these seven LMC clusters may simply be owing to their dynamically young ages or to small-number statistics.

As shown in Fig. 13, the distributions of $A_{\text{rh}}^+ - \log t_{\text{r0}}/t_{\text{iso}}$ for our LMC clusters and the $A_{\text{rh}}^+ - \log t_{\text{r0}}/t_{\text{H}}$ for the Galactic GCs overlap. All seven LMC clusters occupy the dynamically younger part of the sequence defined by the Galactic GCs in the $A_{\text{rh}}^+ - \log t_{\text{r0}}/t_{\text{H}}$ diagram. If we combine our results for BSSs in the LMC

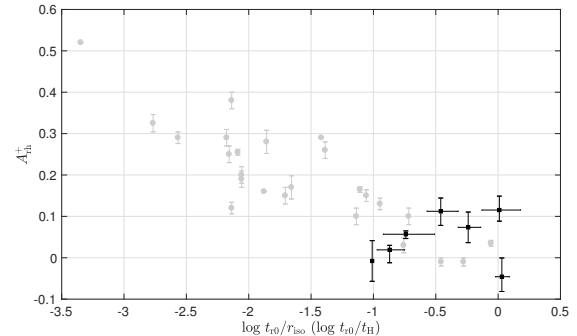


Figure 13. $A_{\text{rh}}^+ - \log t_{\text{r0}}/t_{\text{iso}}$ for BSSs. The $A_{\text{rh}}^+ - \log t_{\text{r0}}/t_{\text{H}}$ diagram for the 25 Galactic GCs (Lanzoni et al. 2016) is also shown.

clusters with that for the Galactic GCs, the resulting Pearson coefficient would still be -0.84 .

4. PHYSICAL IMPLICATIONS

Since most of our clusters have smaller A_{rh}^+ compared with the Galactic GCs, they are also dynamically younger than the GCs. This is consistent with Lanzoni et al. (2016) and Ferraro et al. (2018). Our results thus imply that A_{rh}^+ may be a potential ‘dynamical probe’ for extragalactic clusters at younger ages as well. To underpin this conclusion, studying some globulars with extremely old dynamical ages is essential. As an example, NGC 2019 is likely a core-collapse cluster in the LMC (Meylan & Djorgovski 1987b), which should be sufficiently advanced dynamically (see Fig. 15). Its BSSs should show a very large A_{rh}^+ if the empirical correlation as derived for Galactic GCs also holds for the LMC clusters.

The A_{rh}^+ for our clusters are more dispersed compared with the values for Galactic GCs with equivalent dynamical ages, which may be caused by their large uncertainties. For example, field contamination is estimated by means of Monte-Carlo simulations rather than direct observations of stellar proper motions. The latter method has been employed for GCs since they are closer than the LMC clusters (e.g., Ferraro et al. 2018). The selection of our stellar samples may also have an effect on the radial distributions of stars in some clusters. In addition, the adopted structural parameters may affect our results. We found that if we adopted the structural parameters from the number density profiles rather than from the brightness profiles, A_{rh}^+ will change as well (although the change is very small indeed).

In Fig. 14, we present a direct comparison with the numerical simulations of Alessandrini et al. (2016). In this simulation, A_{rh}^+ for the BSSs of star clusters is controlled by two physical properties, the King central dimensionless potential, W_0 , which defines the initial cen-

Table 6. Calculated total cluster masses (2), average stellar masses (3), central relaxation times (4), half-light relaxation times (5), and A_{rh}^+ for the BSSs (6).

Cluster (1)	$\log M_{\text{tot}}$ (2) [M_{\odot}]	\bar{m} (3) [M_{\odot}]	$\log t_{\text{r0}}$ (4) [yr]	$\log t_{\text{rh}}$ (5) [yr]	A_{rh}^+ (6)
NGC 1831	$4.57^{+0.15}_{-0.12}$	0.37	$8.86^{+0.14}_{-0.17}$	$9.38^{+0.31}_{-0.19}$	$0.1153^{+0.0269}_{-0.0336}$
NGC 1868	$4.31^{+0.05}_{-0.11}$	0.35	$8.21^{+0.10}_{-0.12}$	$8.91^{+0.11}_{-0.19}$	$0.0191^{+0.0312}_{-0.0109}$
NGC 2173	$4.45^{+0.08}_{-0.15}$	0.34	$8.79^{+0.11}_{-0.14}$	$9.54^{+0.19}_{-0.31}$	$0.1123^{+0.0341}_{-0.0321}$
NGC 2203	$4.57^{+0.03}_{-0.05}$	0.33	$9.28^{+0.05}_{-0.06}$	$9.67^{+0.06}_{-0.10}$	$-0.0458^{+0.0357}_{-0.0453}$
NGC 2213	$4.57^{+0.04}_{-0.05}$	0.33	8.25 ± 0.01	$9.06^{+0.09}_{-0.14}$	$-0.0078^{+0.0491}_{-0.0492}$
NGC 1651	4.43 ± 0.05	0.33	$9.06^{+0.08}_{-0.10}$	$9.40^{+0.08}_{-0.10}$	$0.0735^{+0.0370}_{-0.0369}$
ESO 121-SC03	$3.92^{+0.08}_{-0.09}$	0.28	$9.10^{+0.18}_{-0.23}$	$9.33^{+0.12}_{-0.14}$	$0.0568^{+0.0104}_{-0.0081}$

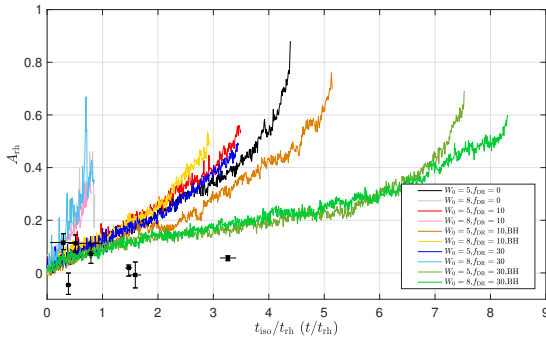


Figure 14. $A_{\text{rh}}^+ - t_{\text{iso}}/t_{\text{rh}}$ diagram for BSSs (black squares). Evolutionary sequences of A_{rh}^+ as a function of t/t_{rh} (Alessandrini et al. 2016) are shown as solid lines.

tral concentration and internal stellar kinematics of star clusters, and the initial retention fraction of dark remnants like neutron stars (NSs) or black holes (BHs), f_{DR} . They found that, for a given W_0 , the initial presence of a large fraction of BHs will have a strong impact on the evolution of A_{rh}^+ . As a result, stellar systems initially without BHs will evolve more rapidly dynamically than those with BHs. The initial concentration also affects A_{rh}^+ at a given dynamical age. A_{rh}^+ is larger in stellar systems with a larger initial concentration, although Alessandrini et al. (2016) only ran two different initial concentration models, characterized by $W_0 = 5$ and $W_0 = 8$.

As shown in Fig. 14, only NGC 1831 may have a relatively high degree of initial concentration level ($W_0 = 8$) and a negligible initial retention fraction of BHs. Given (i) that the deviation of NGC 1831 is small and (ii) the positive result of the Anderson–Darling test, we conclude that the NGC 1831 data point may simply be caused by spurious noise. The other six clusters seem to be consistent with models with a lower initial concentration ($W_0 = 5$) and/or with an initial fraction of BHs ($f_{\text{DR}} = 10, 30, \text{BH}$). Three of the clusters might be dynamically too young to show any dynamical ef-

fects (younger than one half-mass relaxation time). As shown by the simulation, except for the $W_0 = 8, f_{\text{DR}}=0$; $W_0 = 8, f_{\text{DR}}=10$ and $W_0 = 8, f_{\text{DR}}=30$ models, for the other models there is almost no change in A_{rh}^+ before one half-mass relaxation timescale. For three other clusters which are dynamically more advanced ($t_{\text{iso}}/t_{\text{rc}} > 1$), A_{rh}^+ is even significantly smaller than the values indicated by the models.

In clusters with a small A_{rh}^+ , the radial distributions of BSSs may be further affected by dynamical disruption of binary stars. Geller et al. (2013) showed that due to the disruption of wide binaries, the binary frequency will decrease toward the core of the cluster after one crossing time. During the period from one crossing time to one half-mass relaxation time, the radial distribution of binaries will fall toward the cluster’s core region. Subsequently, their radial distribution will exhibit a bimodal morphology, similar to that of BSSs in most GCs. If BSSs inherit the same dynamical history as the binaries, it is possible that they will have a negative A_{rh}^+ . If BSSs form later than most individual stars, their radial distributions may have been shaped when they were born, exhibiting a positive A_{rh}^+ . This is different from Alessandrini et al. (2016). In their simulation A_{rh}^+ is always zero or positive. The binary dynamical disruption effect, combined with the delayed mass segregation due to the presence of BHs, may lead to a very small A_{rh}^+ for a long period, which may explain why some clusters have A_{rh}^+ values that are even smaller than those given by the models. Their low A_{rh}^+ may also indicate that the initial retention fraction of BHs is greater than 30%. The combined effects of binary disruption and the presence of BHs has been studied for NGC 2213 by Li & Hong (2018), who successfully reproduced the non-segregated BSS population in this cluster. Here we find $A_{\text{rh}}^+ = -0.0078$ for its BSSs, which means they are not evolved dynamically at all. A comprehensive study of the effects of BHs and binary disruption in other clus-

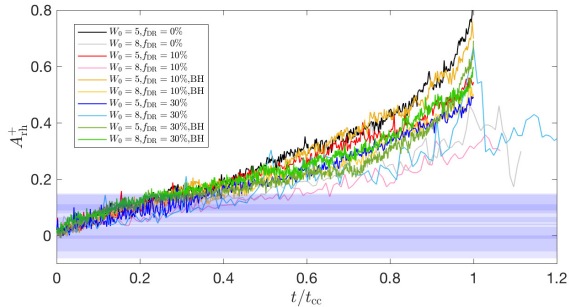


Figure 15. As Fig. 15, but with time normalized to the clusters’ core-collapse time. The calculated A_{rh}^+ ranges for the BSSs are shown as shaded regions.

ters will be explored in a future study (J. Hong et al., in preparation).

We remind the reader that [Alessandrini et al. \(2016\)](#) used the initial relaxation time to scale the dynamical state of the clusters, while in this paper we used the current relaxation time because the initial relaxation time is not measurable. Some uncertainties may have been introduced because of this. In general, we expect that a cluster will have a shorter initial relaxation time because of the subsequent expansion caused by evolutionary mass loss. If so, the actual dynamical age of our clusters, if measured by their initial relaxation time, may be larger than suggested by our current results.

[Alessandrini et al. \(2016\)](#) showed that A_{rh}^+ can be used to evaluate if a cluster has experienced a core-collapse event. By comparing our results with their simulation, we conclude that there is no post-core-collapse cluster among our clusters. In Fig. 15 we show the evolution of A_{rh}^+ to the clusters’ core-collapse time (see [Alessandrini et al. 2016](#), their Fig. 6). The calculated ranges of A_{rh}^+ for the BSSs in our clusters are shown as the shaded bands. Fig. 15 shows that when a star cluster reaches its core-collapse phase, its A_{rh}^+ will increase to at least 0.3, which is greater than A_{rh}^+ derived for any of our clusters. As shown in Fig. 15, all clusters should be younger than 40% of the relevant core-collapse time. In summary, none of these clusters are core-collapse clusters. As shown in [Sun et al. \(2018\)](#), these clusters are not dense enough either to have high stellar collision rates ([Chatterjee et al. 2013](#)). Therefore, most of their BSSs may have been formed through binary evolution.

5. SUMMARY AND CONCLUSIONS

We studied the radial distributions of BSSs in seven LMC clusters with ages spanning from less than 1 Gyr to ~ 7 Gyr. Using the same method employed as [Lanzoni et al. \(2016\)](#) and [Ferraro et al. \(2018\)](#), we identified their A_{rh}^+ and determined their dynamical ages. We found that our clusters are dynamically younger than the Galactic GCs studied by [Lanzoni et al. \(2016\)](#) and [Ferraro et al. \(2018\)](#). Their A_{rh}^+ are also smaller. The $A_{\text{rh}}^+ - \log t_{\text{r}0}/t_{\text{iso}}$ distribution of our clusters is consistent with that of the Galactic GCs, indicating that the radial BSS distributions could potentially be good indicators to measure the dynamical state of younger clusters.

By comparison of our results with the simulations run by [Alessandrini et al. \(2016\)](#), we conclude that most of our clusters may initially have contained a significant fraction of BHs. The presence of BHs may have delayed their mass segregation, leading to a smaller A_{rh}^+ than for star clusters initially without BHs. Our results show that for many of our clusters A_{rh}^+ is close to zero or even negative, which means that their BSSs are almost unevolved dynamically. We suggest that in addition to the presence of BHs, dynamical binary disruption may have shaped the radial distributions of the BSSs. The small A_{rh}^+ values for our clusters also indicate that none have experienced post-core-collapse events, which is expected since our clusters are too young to go through core collapse.

We thank Barbara Lanzoni at Bologna University for providing us with the numerical simulation data. We thank Orsola de Marco at Macquarie University for useful discussions. C. L. is supported by the Macquarie Research Fellowship Scheme. This work was supported by the National Key Research and Development Program of China through grant 2017YFA0402702 (RdG). J. H. acknowledges support from the China Postdoctoral Science Foundation (grant 2017M610694). A. S. is supported by the Natural Sciences and Engineering Research Council of Canada. This work was partly supported by the National Natural Science Foundation of China through grants U1631102, 11373010, 11473037, 11633005, and 11673032. Computations have been done in part on computers of the Silk Road Project and the Laohu (Tiger) supercomputer at the National Astronomical Observatories of the Chinese Academy of Sciences (NAOC).

Facilities: Hubble Space Telescope (WFC3/UVIS and ACS/WFC)

Software: DOLPHOT2.0 ([Dolphin 2016](#))

REFERENCES

- Alessandrini, E., Lanzoni, B., Ferraro, F. R., Miocchi, P., & Vesperini, E. 2016, *ApJ*, 833, 252
- Andronov, N., Pinsonneault, M. H., & Terndrup, D. M. 2006, *ApJ*, 646, 1160
- Baumgardt, H., Parmentier, G., Anders, P., & Grebel, E. K. 2013, *MNRAS*, 430, 676
- Bastian, N., & Niederhofer, F. 2015, *MNRAS*, 448, 1863
- Bressan, A., Marigo, P., Girardi, L., et al. 2012, *MNRAS*, 427, 127
- Chatterjee, S., Rasio, F. A., Sills, A., & Glebbeek, E. 2013, *ApJ*, 777, 106
- Dalessandro, E., Ferraro, F. R., Massari, D., et al. 2013, *ApJ*, 778, 135
- de Grijs, R., Wicker, J. E., & Bono, G. 2014, *AJ*, 147, 122
- Dolphin, A. 2016, *Astrophysics Source Code Library*, ascl:1608.013
- Ferraro, F. R., Pecci, F. F., Cacciari, C., et al. 1993, *AJ*, 106, 2324
- Ferraro, F. R., Beccari, G., Dalessandro, E., et al. 2009, *Nature*, 462, 1028
- Ferraro, F. R., Lanzoni, B., Dalessandro, E., et al. 2012, *Nature*, 492, 393
- Ferraro, F. R., Lanzoni, B., Raso, S., et al. 2018, *ApJ*, 860, 36
- Fiorentino, G., Lanzoni, B., Dalessandro, E., et al. 2014, *ApJ*, 783, 34
- Geller, A. M., de Grijs, R., Li, C., & Hurley, J. R. 2013, *ApJ*, 779, 30
- Geller, A. M., de Grijs, R., Li, C., & Hurley, J. R. 2015, *ApJ*, 805, 11
- Hills, J. G., & Day, C. A. 1976, *Astrophys. Lett.*, 17, 87
- King, I. 1962, *AJ*, 67, 471
- Knigge, C., Leigh, N., & Sills, A. 2009, *Nature*, 457, 288
- Kroupa, P. 2001, *MNRAS*, 322, 231
- Lanzoni, B., Ferraro, F. R., Alessandrini, E., et al. 2016, *ApJL*, 833, L29
- Li, C., de Grijs, R., & Deng, L. 2013, *MNRAS*, 436, 1497
- Li, C., de Grijs, R., Deng, L., & Liu, X. 2013, *ApJL*, 770, L7
- Li, C., de Grijs, R., & Deng, L. 2014, *Nature*, 516, 367
- Li, C., & Hong, J. 2018, *MNRAS*, 476, 5274
- Li, C., Deng, L., de Grijs, R., Jiang, D., & Xin, Y. 2018, *ApJ*, 856, 25
- Li, C., Deng, L., Bekki, K., Hong, J., de Grijs, R., & For, B. Q. 2018, *AJ*, in press
- Marino, A. F., Milone, A. P., Casagrande, L., et al. 2018, *arXiv:1807.05888*
- McCrea, W. H. 1964, *MNRAS*, 128, 147
- McLaughlin, D. E., & van der Marel, R. P. 2005, *ApJS*, 161, 304
- Meylan, G. 1987, *A&A*, 184, 144
- Meylan, G., & Djorgovski, S. 1987, *ApJL*, 322, L91
- Milone, A. P., Bedin, L. R., Piotto, G., & Anderson, J. 2009, *A&A*, 497, 755
- Milone, A. P., Piotto, G., Bedin, L. R., et al. 2012, *A&A*, 540, A16
- Milone, A. P., Marino, A. F., Di Criscienzo, M., et al. 2018, *MNRAS*, 477, 2640
- Sandage, A. R. 1953, *AJ*, 58, 61
- Simunovic, M., Puzia, T. H., & Sills, A. 2014, *ApJL*, 795, L10
- Spitzer, L. 1987, Princeton, NJ, Princeton University Press, 1987, 191 p.,
- Sun, W., Li, C., de Grijs, R., & Deng, L. 2018, *ApJ*, 862, 133
- Yang, Y., Li, C., Deng, L., de Grijs, R., & Milone, A. P. 2018, *ApJ*, 859, 98